JOURNAL OF COMPUTATIONAL PHYSICS 51, 291–312 (1983)

Experiments with Some Low-Order Finite Element Schemes for the Navier–Stokes Equations

M. J. P. CULLEN

Forecasting Research Branch,
Meteorological Office, Bracknell, Berkshire, England

Received July 2, 1982; revised December 7, 1982

It is shown how a consistent finite element approximation to the Navier–Stokes equations can be constructed on a general grid using an arrangement equivalent to the MAC stencil. It is known that the standard Galerkin construction does not give a consistent result unless at least quadratic velocities are used in this type of element. However, the use of either a finite difference approximation to the pressure gradient term or a Galerkin scheme equivalent to a vorticity method appears to give a consistent scheme. Both alternatives are tested, and the vorticity method is shown to be superior.

1. INTRODUCTION

Approximation of incompressible flows by the finite element method is currently a very active field of research. Since many of the applications of incompressible flow codes involve complex geometry, the finite element method is a natural candidate. Because the incompressibility constraint forces some of the calculation to be implicit, the finite element method is a much stronger competitor for finite difference schemes than it is in problems where fully explicit finite differences can be used. However, much work remains to be done in understanding, for instance, under what conditions finite element methods work well for transient flows and the relationships between primitive variable and vorticity formulations, and between finite element and other methods. A recent review paper by Hughes *et al.* [1] discusses some of these issues and lists many of the references to work in this area.

In this paper we study some lower-order finite element approximations. It is desirable to use a low-order scheme because finite element schemes may be very expensive in computer time and storage, particularly in three dimensions. The most common such scheme is to use a bilinear or trilinear approximation to the velocity field and a piecewise constant approximation to pressure. This element was used in [1] and by Gresho *et al.* [3] among many others. An alternative scheme was recently proposed by DiCarlo and Piva [8], based on the finite difference MAC stencil of Harlow and Welch [7]. They demonstrated an apparent advantage in accuracy over the scheme used in [3] for a rectangular grid. However, it is not easy to apply such a scheme to an arbitrary grid defined by an isoparametric coordinate transformation.

0021-9991/83 $3.00

It is possible to construct a Galerkin algorithm in this case, in the way discussed by Raviart [9], but it does not give convergent results. In [8] the scheme was therefore only advocated for use with global coordinate transformations, for instance, those of Thames *et al.* [6]. In this paper we examine two methods of obtaining a convergent result with this element. One method is to use a finite difference operator instead of the Galerkin approximation to the pressure gradient term. The other is to use a full

R is the Reynolds number and the remaining notation is standard. The structure of incompressible flow in two dimensions is simpler than in three, and the algorithms are described for this case. The extension to three dimensions is discussed separately. Only two-dimensional computations will be presented.

We now introduce a low-order finite element scheme for (2.1) with the variables defined in a way analogous to the finite difference MAC stencil. This scheme was described by Dicarlo and Piva [8], and proposed for use in general geometry by using a global coordinate transformation. In this paper, we develop ways of using it with the standard local isoparametric mapping.

The domain Ω is subdivided into quadrilaterals. The global coordinates (x, y) are transformed in the usual way into local coordinates (ξ, η) by a piecewise bilinear transformation:

$$x = x(\xi, \eta), \qquad y = y(\xi, \eta).$$

Each element is transformed to a square $(0, 1) \times (0, 1)$ in the (ξ, η) coordinates. The local coordinates are non-orthogonal. The velocity field is approximated in terms of the mass flux across element sides. The nodal parameters are thus the integrated normal fluxes across the sides, and are assumed to be located at midside nodes. There are four degrees of freedom per element. The flux across the sides $\xi =$ constant is assumed to be linear in ξ and independent of η, and vice versa. Provided the elements remain non-singular, this means that velocity components in two different directions are defined everywhere in each element, giving a representation of the velocity field in which the tangential velocity only is discontinuous across element boundaries. The prescribed variation in the mass fluxes establishes a logical connection between opposite sides of quadrilaterals. The structure of this connection on an arbitrary mesh is illustrated in Fig. 1. There is no need for the mesh to be logically rectangular.

The definition of the velocity field in terms of mass fluxes means that the continuity equation (2.2) can be approximated by

$$\sum_{i=1}^{4} \mathbf{m}_i \cdot \hat{\mathbf{ds}}_i = 0, \tag{2.3}$$

where the sum is taken over the four sides of each element in turn and the vector $\mathbf{m}$ represents the mass flux.

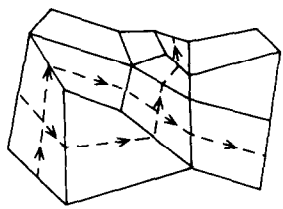

FIG. 1. Logical structure of velocity representation.

The velocity field implied by this representation has covariant components in the (ξ, η) directions $(n\alpha^{-1/2}, n\gamma^{-1/2})$, where (m, n) are the fluxes and α, γ are components of the metric tensor of the bilinear coordinate transformation, defined in full by

$$\alpha = x_\eta^2 + y_\eta^2, \qquad \beta = x_\xi x_\eta + y_\xi y_\eta, \qquad \gamma = x_\xi^2 + y_\xi^2,$$
$$J = x_\xi y_\eta - y_\xi x_\eta. \tag{2.4}$$

The contravariant components can be calculated in the usual way. The fluxes (m, n) can be written in the form

$$\left(\sum m_i \lambda_i(\xi), \sum n_j \mu_j(\eta)\right), \tag{2.5}$$

where λ_i are basis functions linear in ξ and independent of η, and μ_j vice versa.

Up to this point, this construction could equally be carried out in three dimensions. In two dimensions, however, we can proceed further by identifying the fluxes (m, n) with the derivatives $(-\partial\psi/\partial\eta, \partial\psi/\partial\xi)$ of a discrete streamfunction ψ, where ψ is bilinear in ξ and η on each element and can be written in the form

$$\sum \psi_n \chi_n(\xi, \eta), \tag{2.6}$$

where χ_n are piecewise bilinear basis functions equal to unity at one corner node and zero at the remainder. The mass fluxes associated with χ_n are shown in Fig. 2. This set of fluxes forms a member of a divergence-free basis for the mass fluxes in the sense of [10, 11]. The Cartesian components of the velocity field $\mathbf{u}$ are given by

$$u = \frac{1}{J}\{\psi_\xi x_\eta - \psi_\eta x_\xi\},$$
$$v = \frac{1}{J}\{\psi_\xi y_\eta - \psi_\eta y_\xi\}. \tag{2.7}$$

Note that these components are not linear in ξ and η.

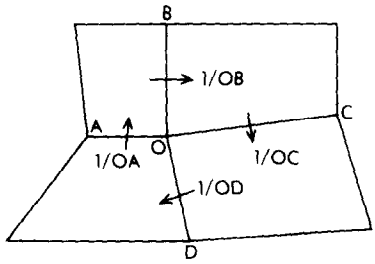

FIG. 2. Local basis for weakly solenoidal space J_h.

This representation is different from that used by Dicarlo and Piva [8]. This is because their specification of the contravariant components of velocity is sufficient to ensure continuity of mass flux if the coordinate transformation is C^1, as are those that they use. Since this isoparametric transformation is not C^1, the definition here has to be directly in terms of mass fluxes.

The pressure in this element is naturally taken as piecewise constant at element

(i) Given initial midside fluxes (m, n) satisfying (2.3) calculate corner nodal values of the streamfunction ψ by direct integration.

(ii) Calculate an approximate piecewise bilinear vorticity field using the Galerkin method with test functions χ_n.

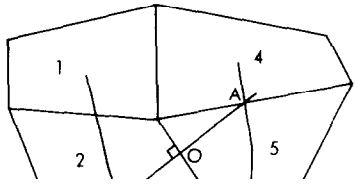
1
4
A
2
O
5

(iii) instead of (2.16), solve the pair of equations

$$\int_\Omega \frac{1}{J} |-(\gamma\chi_{n\eta} - \beta\chi_{n\xi})(m_{t+\Delta t} - m_{t\ \Delta t}) + (\alpha\chi_{n\xi} - \beta\chi_{n\eta})(n_{t+\Delta t} - n_{t-\Delta t})| \, d\xi \, d\eta$$

$$= 2\Delta t \int \frac{(\alpha\gamma - \beta^2)}{\quad} \zeta_{\cdot}(-\gamma_{\cdot\cdot\cdot}\psi_{\cdot} + \psi_{\cdot}\gamma_{\cdot\cdot\cdot})_{\cdot} + \frac{1}{\quad} |\zeta_{\cdot}(\alpha\gamma_{\cdot\cdot\cdot} - \beta\gamma_{\cdot\cdot\cdot})$$

where the local isoparametric coordinates are (ξ, η, α). Equation (2.15) can then be written as

$$\int_{\partial\Omega} \chi_n \mathbf{u} \cdot \mathbf{ds} - \int_{\Omega} \mathbf{u} \times \nabla\chi_n \, d\Omega = \int_{\Omega} \zeta\chi_n \, d\Omega.$$

It is then straightforward to construct (2.16); and the rest of the hybrid finite difference algorithm.

While the vorticity-based algorithm (2.19) can still be written down, the pair (2.19), (2.20) do not contain sufficient equations if (2.19) is only written for interior nodes; even though it is now a vector equation. This difference is associated with the difficulty of choosing boundary conditions on the vector potential to allow a three-dimensional velocity field to be constructed from the vorticity field. This problem has not yet been satisfactorily resolved except in simple geometry.

3. Experiments

3.1. *Introductory Remarks*

In this section we demonstrate the validity of the two algorithms using the MAC-type finite element scheme by applying it to two standard test problems where the results are known from careful high-resolution computations. These are, unfortunately, steady flow simulations and can only provide a limited test of a transient code. However, inconsistency in the algorithm is still likely to show up in a steady case; it is hoped to test the algorithms on transient problems in the future. Since most of the difficulties with this sort of element only appear with a distorted grid, one of the tests involves non-trivial geometry. In order to estimate the resolving power the calculations are intentionally performed with rather limited resolution, since a duplication of the known solution with a very fine grid would not give any information about the cost-effectiveness of the scheme.

3.2. *Driven Cavity Problem*

This standard test consists of calculating the steady two-dimensional flow in a square box $(0, 1) \times (0, 1)$ driven by the lateral movement of the lid. This was used to test the finite element MAC scheme in [8]. Results for a selection of Reynolds numbers have been reviewed by Olson and Tuann [16]. Very accurate reference results have been computed for $Re = 1400$ and 2000 by Winters and Cliffe [17]. As an initial test, results were computed for $Re = 1$ to check against those of [8], and identical results were obtained. The flow at $Re = 100$ and 400 was then computed using a stretched 11×11 rectangular grid with values of x on each row and y on each column of (0.00, 0.02, 0.08, 0.18, 0.32, 0.50, 0.68, 0.82, 0.92, 0.98, 1.00). Reynolds number considerations suggest that the boundary layers should be just resolved for $Re = 100$ but not for $Re = 400$.

The computations were carried out using both the vorticity projection algorithm

(2.19) and the finite difference pressure gradient (2.17). The latter was implemented with both the algorithm (2.16) for the nonlinear term and with a two-stage scheme (2.18). When (2.19) is used the pressure is recovered as a bilinear function by solving the Poisson equation derived from (2.21). The result is the dynamic pressure and interpolated values of u and v are used to estimate the static pressure. The pressure is normalised by its value at the midpoint of the side opposite the sliding lid.

The transient equations were integrated forward in time till apparent steady state. However, there is always the possibility of some residual error when comparing with solutions given by a steady-state code such as that in [17]. Cross sections of the results are given in Figs. 4 to 13, since a quantitative comparison is easier than with a two-dimensional field. However, these have to be treated with some caution, since the grid resolution normal to the cross section is very low. In both figures and text the results using the vorticity projection are denoted as V and using the finite difference projection with single and two-stage advection as F1 and F2.

At $Re = 100$ the results are shown in Figs. 4 to 8 and can be compared with those summarized in [16]. Reference [16] gives values of the streamfunction at the vortex center ranging from 0.0784 to 0.1022, with the latter considered the best result. The best value for the vorticity at the vortex center is 3.155 and for the normalised

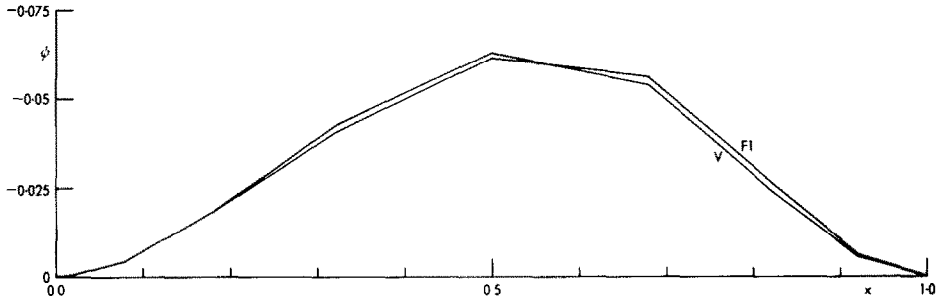

FIG. 4. Streamfunction along horizontal center line, $Re = 100$. V: Vorticity projection; F1: finite difference.

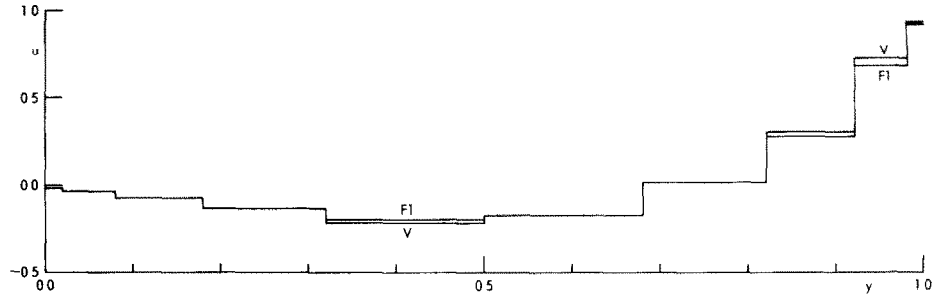

FIG. 5. u velocity along vertical center line, $Re = 100$. Notation as in Fig. 4.

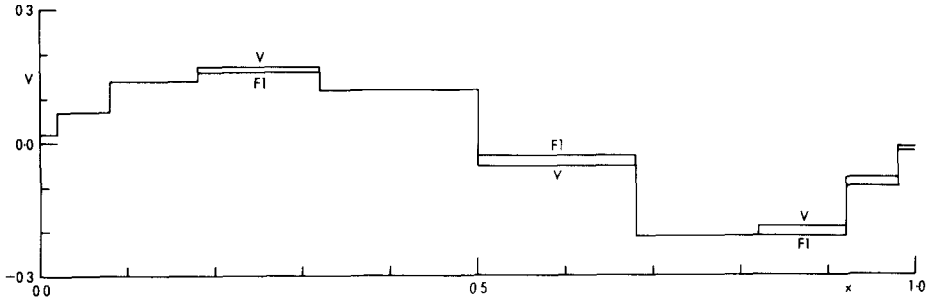

FIG. 6. v velocity along horizontal center line, Re = 100. Notation as in Fig. 4.

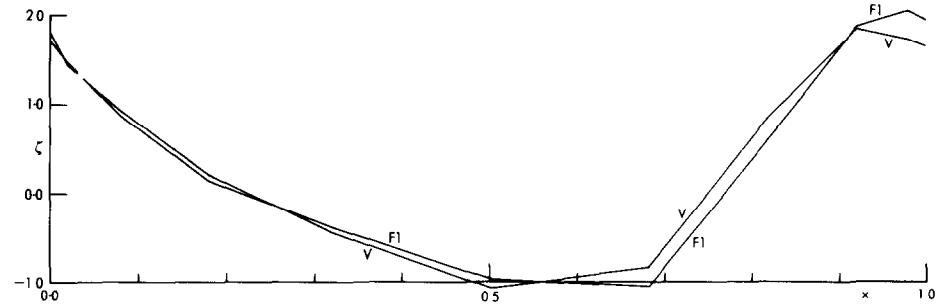

FIG. 7. Vorticity along horizontal center line, $Re = 100$. Notation as in Fig. 4.

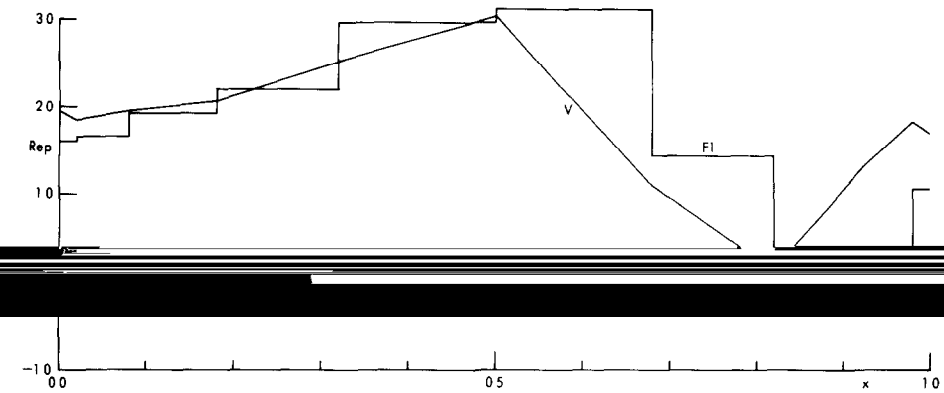

FIG. 8. Pressure along horizontal center line, $Re = 100$. Notation as in Fig. 4.

pressure 0.0922. The values obtained in the present calculations are, for the streamfunction, 0.097 (V), 0.095 (F1), 0.094 (F2), for the vorticity, 4.23 (V), 3.88 (F1), 4.04 (F2), and for the pressure, 0.091 (V), 0.086 (F1), 0.087 (F2). Since in F1 and F2 the pressure is not calculated at the same positions as the streamfunction, the extreme value closest to the vortex center is given. The streamfunction values obtained for the reverse eddies in the lower corners, denoted LL and LR, are

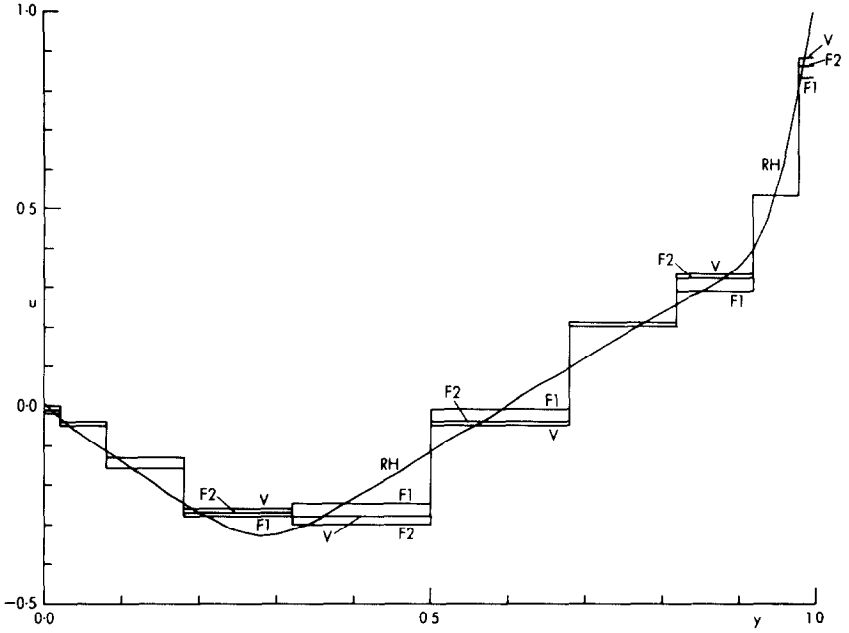

FIG. 10. u velocity along vertical center line, Re = 400. Notation as in Fig. 9.

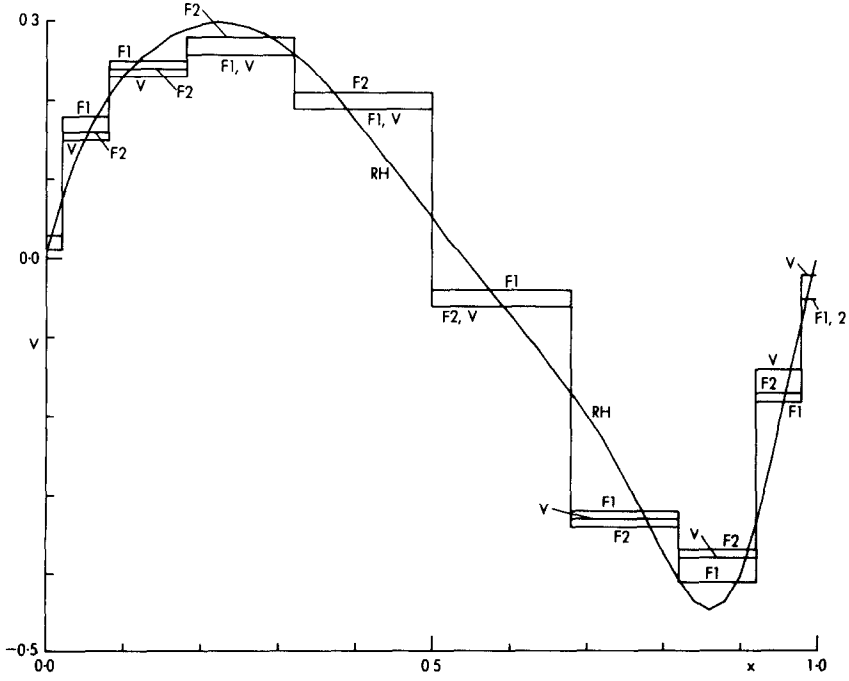

FIG. 11. v velocity along horizontal center line, $Re = 400$. Notation as in Fig. 9.

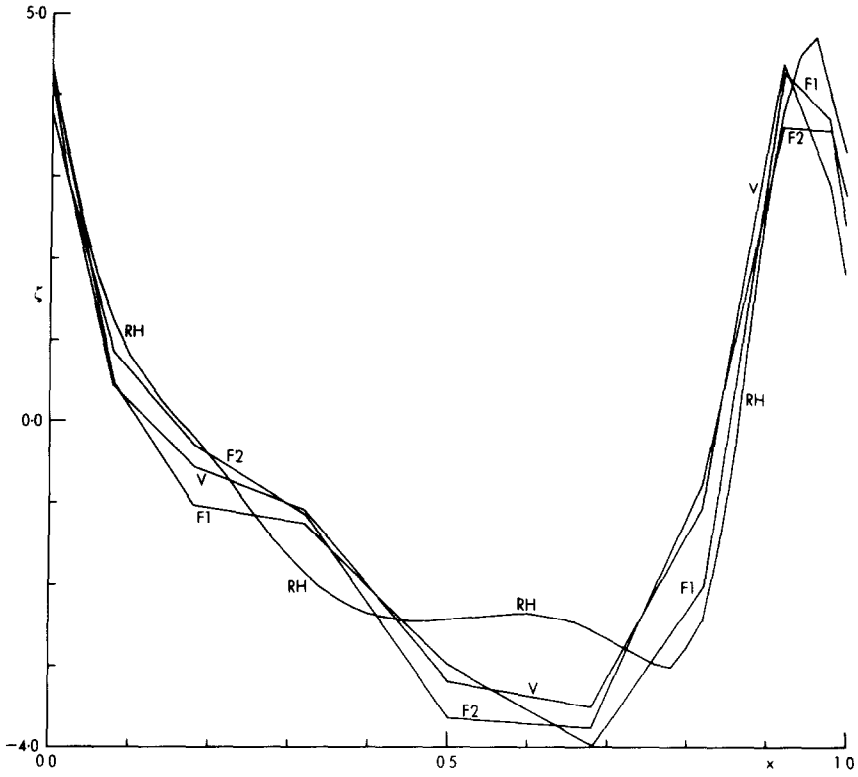

FIG. 12. Vorticity along horizontal center line, Re = 400. Notation as in Fig. 9.

are 1.4×10^{-6} (LL) and 74×10^{-5} (LR) using V; 10×10^{-6} and 29×10^{-5} using F1; and 76×10^{-6} and 14×10^{-5} using F2. The value for LR given by RH is about 5×10^{-4}. The graph of u velocity (Fig. 10) again shows intermediate results between RH and RL, with V slightly superior. The graph of v velocity (Fig. 11) shows the same story except that F1 and F2 are slightly superior. The vorticity results (Fig. 12) show the effect of the reduced resolution. The results obtained here are clearly inferior to those in [17]. This is because there is non-trivial structure in the vorticity field in the centre of the cavity, and this cannot be captured by the grid. It is noteworthy that the different algorithms used here all give very similar wrong results. Near the wall $x = 1$ the grid does have enough resolution, and the peak vorticity is captured in V and F1 better than in RL. The resolution of RL and V normal to the wall is similar in the boundary layer in terms of elements, but V uses fewer degrees of freedom. This suggests that the arrangement of variables on the grid has produced the improved resolution claimed in [8].

The pressure results (Fig. 13) from F1 and F2 are a little better than RL but well short of the accurate solution given by RH. Those from V show an accurate peak value, but wrong behaviour near $x = 1$. As in the case of $Re = 100$, this is caused by

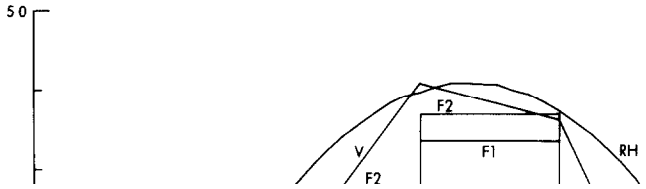
50
F2
F1
V
F2
RH

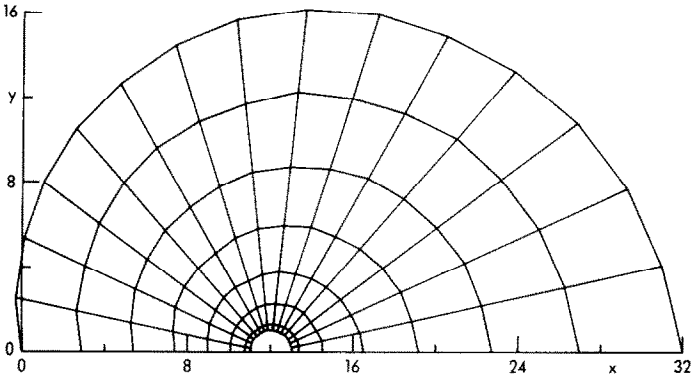

FIG. 14. Finite element mesh used for cylinder simulations.

calculating a streamfunction at inflow points on the grid and deriving fluxes from it. These were held constant through the integration. At outflow the condition $\partial \mathbf{u} \cdot \mathbf{n}/\partial n = 0$ was enforced by equalising the normal velocity across the sides of the outermost element. The symmetry condition was enforced as $\psi = 0$, and the cylinder surface as $\partial\psi/\partial n = 0$. The region of integration was chosen as in [15] to include all the likely region of disturbed flow at the values of Reynolds number used. However, as discussed recently by Fornberg [5], the boundary condition has to be imposed at a distance much further out than the region of disturbed flow. The experiments in [5] also indicate that the best boundary condition to use involves an analytic expansion for the far field stream function. Since the boundary conditions used here are not quite the same as used in either [5] or [15], there may be discrepancies in the results.

The models were integrated first to approximate steady state with $Re = 1$, and then successively increasing Re to 5, 7, 10, 20 and 40. Results are shown here for $Re = 7$, 10, 20 and 40 in the form of graphs of ζ and p along the cylinder surface. This allows a quantitative comparison with [15]. In the case of the vorticity projection, values of p are recovered as described in Section 2. Values are therefore obtained on the cylinder wall directly. In the finite difference projection, values are obtained at element centroids. No extrapolation procedure was used to generate values on the wall, since attempting to do so did not give more accurate results. Integrations were carried out using the vorticity projection on a 15×7 element grid, and the finite difference projection on 15×7 and 22×10 grids. These are denoted by V, FL and FH, respectively. These are compared with the results of [15]; their 42-element grid results are denoted RL, and the 78-element grid results RH. They are also compared with the finite difference results of [18], denoted RF.

At $Re = 7$, the vorticity results (Fig. 15) show that only FH of the integrations done here produces a recirculating wake like the methods of [15]. This is indicated by a change of sign of the vorticity on the cylinder surface near the trailing edge. The magnitude of the region given by FH is much less than that given by RH and RF. Though the calculations here differ from [15] in imposing symmetry, this should not

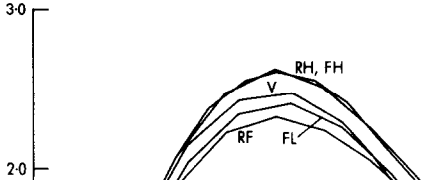
3·0
2·0
RH, FH
V
RF
FL

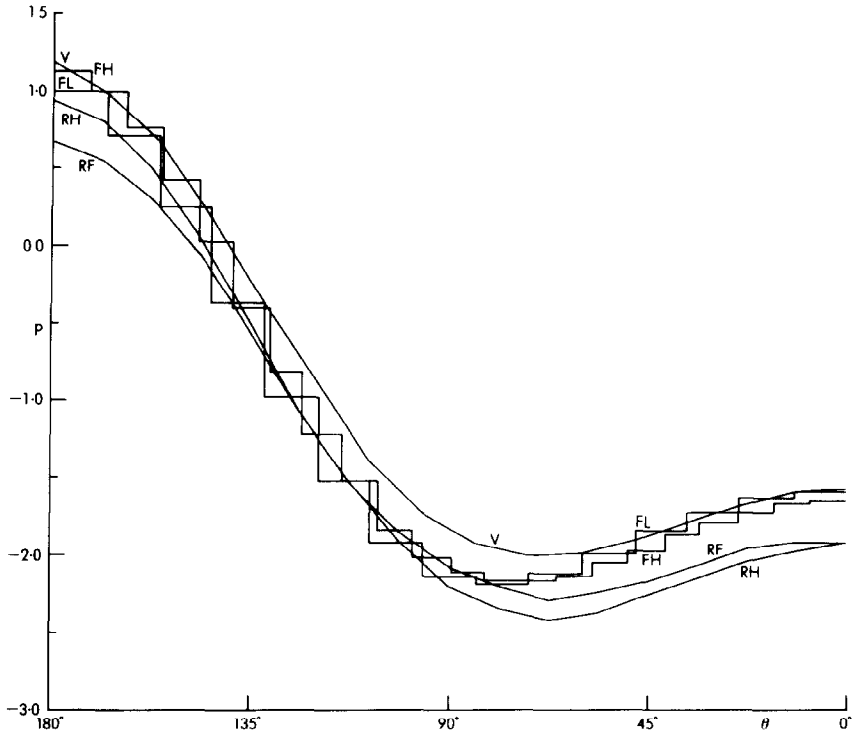

FIG. 16. Pressure along cylinder surface, $Re = 7$. Notation as in Fig. 15.

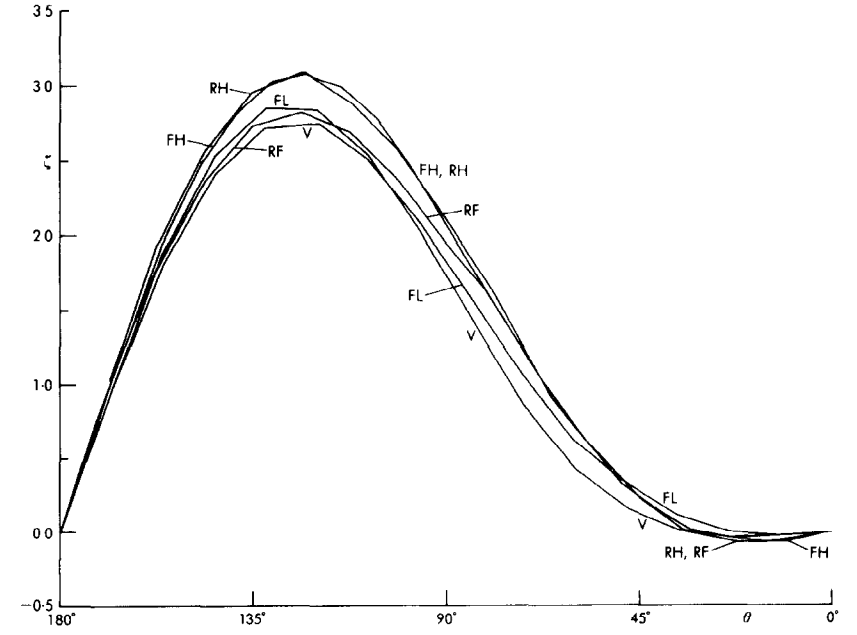

FIG. 17. Vorticity along cylinder surface, $Re = 10$. Notation as in Fig. 15.

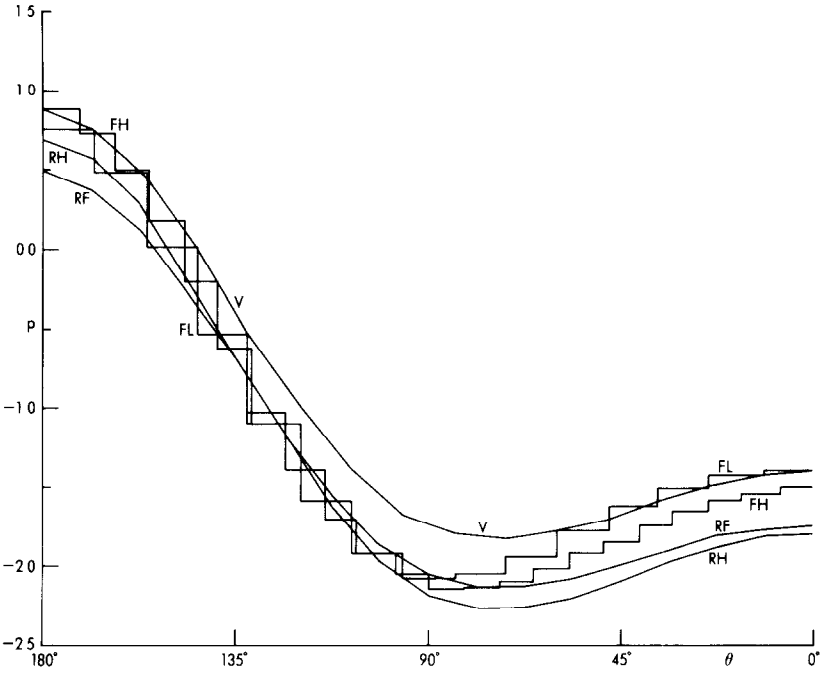

FIG. 18. Pressure along cylinder surface, $Re = 10$. Notation as in Fig. 15.

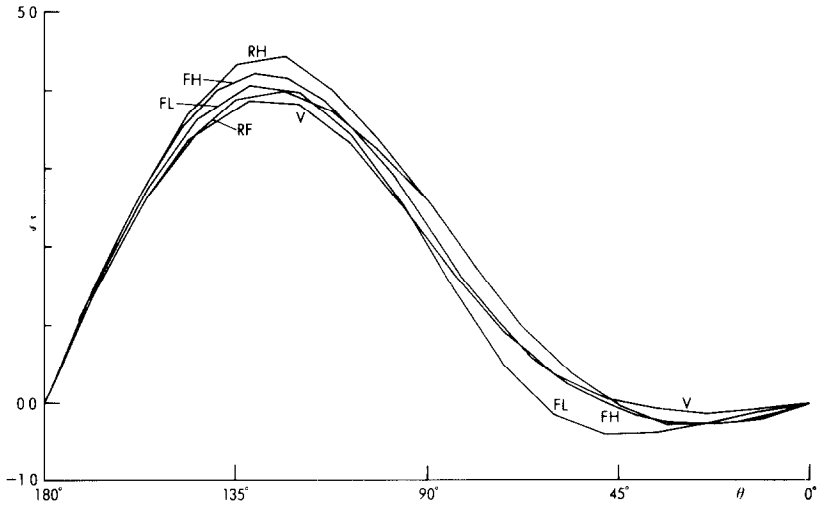

FIG. 19. Vorticity along cylinder surface, $Re = 20$. Notation as in Fig. 15.

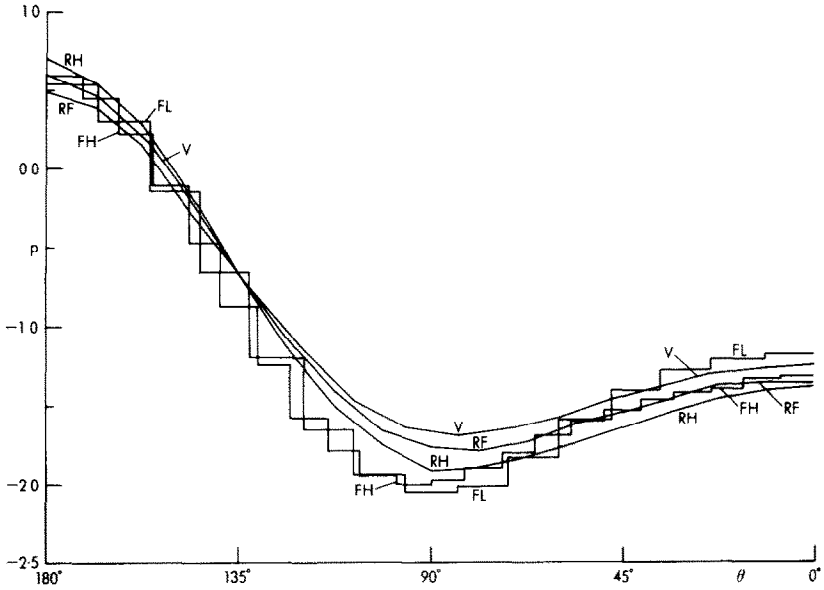

FIG. 20. Pressure along cylinder surface, $Re = 20$. Notation as in Fig. 15.

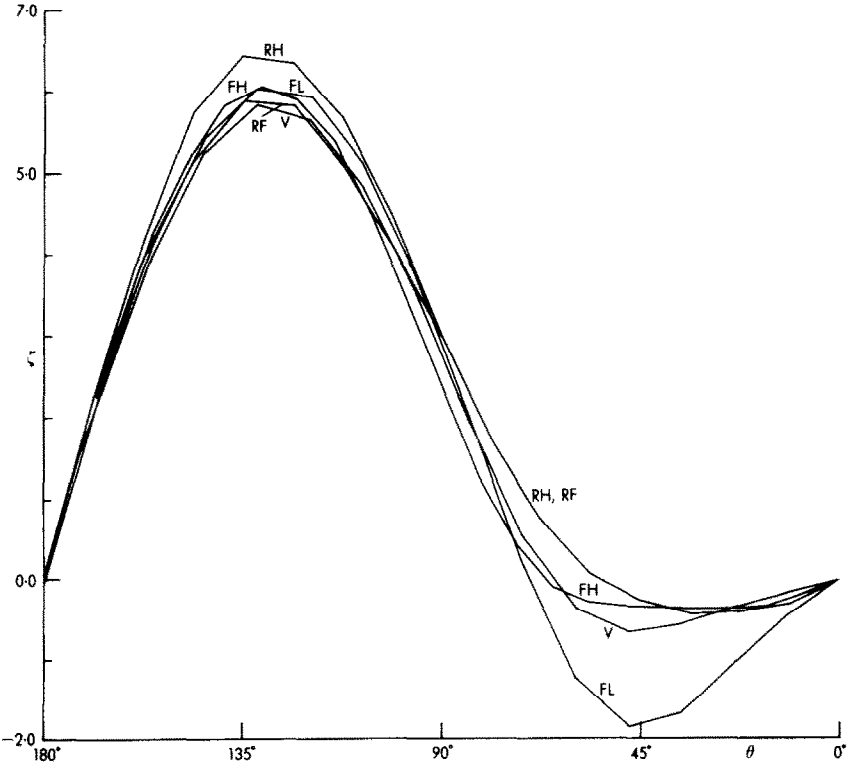

FIG. 21. Vorticity along cylinder surface, $Re = 40$. Notation as in Fig. 15

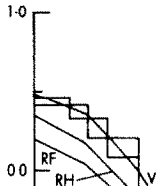
1·0
0·0
RF
RH
NV

the method as a vorticity method or by using a finite difference approximation to the pressure gradient term. In irregular geometry the vorticity-based method works better. This suggests that such methods may have advantages. In the problem with regular geometry, the results were insensitive to this choice of algorithm. However, all the algorithms used the same approximation to the continuity equation, and it is possible that this was the major source of error. Otherwise, the conclusion would be that grid design is much more important than choice of algorithm.

In some problems, the finite element method is successful even on coarse grids because the result it gives is an exact best fit in some sense (e.g., in the energy norm). In the problems solved here the answers on coarse grids do not seem to be exact best fits in any useful sense, so that there is no possibility of recovering much extra information by post-processing.

ACKNOWLEDGMENTS

This study was carried out while the author was visiting the Department of Mathematics, University of California, Berkeley, under the sponsorship of the Centre for Pure and Applied Mathematics. The author benefited greatly from regular discussions with Professor Alexandre Chorin, and with Dr. P. M. Gresho and his group at the Lawrence Livermore Laboratory.

REFERENCES

1. T. J. R. HUGHES, W. K. LIU, AND A. BROOKS, *J. Comput. Phys.* **30** (1979), 1–30.
2. M. J. P. CULLEN, *J. Comput. Phys.* **51** (1983), 273–290.
3. P. M. GRESHO, R. L. LEE, AND C. D. UPSON, *Adv. Water Resources* **4** (1981), 175–184.
4. M. J. P. CULLEN AND K. W. MORTON, *J. Comput. Phys.* **34** (1980), 245–267.
5. B. FORNBERG, *J. Fluid Mech.* **98** (1980), 819–855.
6. F. C. THAMES, J. F. THOMPSON, C. W. MASTIN, AND R. L. WALKER, *J. Comput. Phys.* **24** (1977), 245–273.
7. F. H. HARLOW AND J. E. WELCH, *Phys. Fluids* **8** (1965), 2182–2189.
8. A. DICARLO AND R. PIVA, *Comput. & Fluids* **8** (1980), 225–241.
9. P. A. RAVIART, *Springer Lecture Notes in Physics* **91** (1977), 27–47.
10. D. F. GRIFFITHS, *Internat. J. Numer. Methods Fluids* **1** (1981), 323–346.
11. M. FORTIN, *Internat. J. Numer. Methods Fluids* **1** (1981), 347–364.
12. A. J. CHORIN AND J. E. MARSDEN, "A Mathematical Introduction to Fluid Mechanics," Springer-Verlag, New York, 1979.
13. A. J. CHORIN, *Math. Comp.* **23** (1968), 341–354.
14. D. C. JESPERSEN, *J. Comput. Phys.* **16** (1974), 383–390.
15. S. Y. TUANN AND M. D. OLSON, *Comput. & Fluids* **6** (1978), 219–240.
16. M. D. OLSON AND S. Y. TUANN, *J. Comput. Phys.* **29** (1978), 1–19.
17. K. H. WINTERS AND K. A. CLIFFE, UKAEA Report R9444, Harwell, Oxfordshire, England, 1979.
18. S. C. R. DENNIS AND G Z. CHANG, *J. Fluid Mech.* **42** (1970), 471–489.